Study on the structural evolution and heat transfer performance of Cu supported on regular morphology CeO$_2$ in CO catalytic combustion and chemical looping combustion

Junqin Huang [a,b], Huan Liu [a], Chenhang Zhang [a], Feng Bin [a,b,*], Xiaolin Wei [a,b], Running Kang [a,b], Shaohua Wu [c,**]

[a] State Key Laboratory of High-Temperature Gas Dynamics, Institute of Mechanics, Chinese Academy of Sciences, Beijing, 100190, PR China
[b] School of Engineering Science, University of Chinese Academy of Sciences, Beijing, 100049, PR China
[c] School of Energy and Power Engineering, Dalian University of Technology, Dalian, 116024, PR China

ARTICLE INFO

ABSTRACT

Chemical looping combustion (CLC) and catalytic combustion (CC), which are potential technologies to promote CO→CO$_2$ efficient conversion and energy conservation for the steelmaking off-gas, are investigated in reaction activity, structure evolution catalysts/oxygen carriers (OCs) and energy recovery using Cu/CeO$_2$ materials. Activity results suggest that the rod-shaped samples with well-defined (100) crystal faces exhibit higher activity than the sphere-shaped samples with (111) crystal faces, obtaining the optimized copper content of 3 wt%. IR spectra confirmed the proposed reaction pathway that the CO adsorbed on copper sites (Cu$^+$–CO) at the Cu–Ce interface reacts with adjacent surface lattice oxygen. The gaseous oxygen continuously migrates to the external surface of materials, thus resulting in strongly exothermic CO self-sustained combustion during CC. Such a violent reaction does not cause obvious evolution of chemical composition, crystalline phase and structure. Since the active lattice oxygen is gradually consumed but not replenished by external gaseous O$_2$ in time, CO combustion is not self-sustained during CLC. Therefore, the reduction cycle is no longer confined to the surface of the material but penetrates deep into its body, which accelerates Cu$^+$ enrichment at the surface and leads to irreversible sintering and agglomeration of the material.

1. Introduction

The steel industry is considered the world's largest energy consuming industry and a major source of greenhouse gas emissions (Igalavithana et al., 2020). About 70% of global steel production uses the oxygen top blown converter method to remove excess carbon from molten iron, which generates a large amount of CO by-products during this process (Wu and Zhou, 2022). Due to the periodicity of the oxygen top blowing converter method, the concentration of CO varies with its periodic changes. CO that meets the recovery conditions (CO > 30 vol% and O$_2$ < 2 vol%) is recycled into the gas storage tank (Kim et al., 2022). CO that does not meet the recycling conditions is first cooled through the evaporative cooling flue, and then ignited and emitted into the atmosphere through methane, resulting in excessive carbon dioxide emissions (including methane combustion) and energy waste (including sensible heat loss from the evaporative cooling flue) (Lian et al., 2022), which undoubtedly exacerbates the high pollution and high energy consumption attributes of the steel industry.

In order to realize the goals of carbon dioxide emission peak before 2030, carbon neutral before 2060 in China, and sustainable development, catalytic combustion (CC) (Mrabet et al., 2012) and chemical chain combustion (CLC) technologies (Sun et al., 2023b; Wu et al., 2020) have received significant research attention to promote energy recovery and CO$_2$ emission reduction. For CC, the CO/air can be ignited at low temperatures in the sole reactor, where the abrupt acceleration of the surface reaction rate causes thermochemical runaway, culminating in the phenomena of CO self-sustaining catalytic combustion (Bin et al., 2019). CLC is an alternative combustion scheme that uses a new

"unmixed combustion" mode to separate fuel and air into two interconnected reactors for reaction, avoiding mixed combustion (Adánez and Abad, 2019). For CLC, use fuel and air reactors to avoid direct contact between CO and air. The oxygen carrier (OCs) is transported to the fuel reactor to react with CO, and the OCs are reduced. Then, the oxygen carrier (OCs) is transported to the air reactor to react with O_2 to fill the oxygen vacancies in the OCs (Long et al., 2021). After regeneration, it is then transported again to the fuel reactor for the next redox cycle. As a result, the outlet dry gas from fuel reactor is almost pure CO_2 without N_2 (Lin et al., 2020). Optimization of CC and CLC requires catalysts/OCs that exhibit high reaction rates (Zuo et al., 2023). The typical copper cerium bimetallic material (Cu/CeO$_2$) has a high catalytic activity due to its synergistic enhancement performance (Liu et al., 2023b). Taking scientific acceptance and commercialization, compared to expensive precious metal catalysts, inexpensive transition metal catalysts have gained favor (Gao et al., 2023; Jia et al., 2022). Understanding the impact of reaction activity and the structural evolution of catalysts/OCs on durability is crucial for energy recovery in CC and CLC processes, as this is the original intention of heat recovery or CO_2 capture in the steelmaking process.

The reaction behavior including structure-activity relationship and stable active centers is very important for CC and CLC. Our previous studies have shown that pure CeO$_2$ or pure CuO has poor activity, but a small amount of copper dispersed on the surface of CeO$_2$ can also greatly enhance its activity (Zhao et al., 2015). The structure activity relationship of Cu–Ce composite oxide catalysts is mainly reflected in the changes in chemical valence states, morphology and structure, as well as the interactions between support active components, etc. In terms of chemical valence state composition and change, the outer electronic structure of the rare earth element Ce layer is $4f^1 5d^1 6s^2$, which has two stable valence states of $+3$ and $+4$ after electron loss. It is easy to realize the storage and release of oxygen through the mutual conversion between Ce^{3+} and Ce^{4+} ions, and is a better oxygen storage body. Yao et al. studied the CO oxidation reaction on CuO/CeO$_2$ catalysts and found that both Ce^{4+}/Ce^{3+} and Cu^{2+}/Cu^+ electron pairs participate in the catalytic cycle. The active site Cu^+ mainly provides adsorption sites for CO, while the active oxygen required during the CO oxidation reaction is mainly provided by CeO$_2$. Therefore, the catalyst activity will be improved under the synergistic effect of Cu–Ce solid solution (Ren et al., 2022). The catalytic activity of Cu/CeO$_2$ in the ignition process is mainly determined by the active site: dispersed CuO$_x$ on the surface of Ce > CuO$_x$ in the catalyst body > pure CuO$_x$ (Wang et al., 2022; ZHAO et al., 2015). To improve the durability and increase the life of active CuO$_x$ for CLC, the CeO$_2$ as support decreases the operation temperature and preserves the OCs through multiple reduction and oxidation cycles, but lowers the oxygen capacity of the overall sample (Sun et al., 2023a). The dispersed CuO$_x$ on the surface of the carrier and adjacent oxygen vacancies contribute to the improvement of activity, as Cu^+ can act as a chemical adsorption/activation site for CO molecules and surface oxygen molecules (Chen et al., 2023; Liu et al., 2023a). Because the reaction behavior attained in CC and CLC varies significantly under testing conditions, it is necessary to keep the effects of experimental factors as the smallest as possible.

As strongly exothermic and fast gas-solid phase catalytic reactions, the CC allows oxidizing CO to CO_2 directly and producing heat according to $2CO + O_2 \rightarrow 2CO_2 + 12.64$ MJ/Nm^3 (283 kJ/mol-CO). For CLC, although the reaction of OCs with CO and O_2 is carried out in two separate reactors, these two steps are exothermic reaction (Sun et al., 2023a). Currently, particular focus is placed on the structure evolution of catalysts/OCs under such violent reactions, including elemental migration, morphological changes and changes of chemical components, which in turn limit the activity (Cho et al., 2005). Hua et al. (2013) demonstrated that the morphologies and crystal phases remained the Cu$_2$O nanocrystals of CC, but the reaction maintained under mild conditions (2 vol% CO). CO reacts more readily with lattice oxygen in OCs at higher temperatures, however this also exacerbates its

agglomeration, leading to increased crystallinity, denser particle structure and redistribution of the crystalline phase Chen et al. (2022) Compared with traditional flame combustion methods, CC reduces ignition temperature, accelerates combustion rate, improves burnout characteristics and heat release rate, while CLC regulates the release of heat energy in an orderly manner due to the role of oxygen release from OCs, reduces irreversible losses and effectively realizes the stepwise utilization of fuel chemical energy (Zhao et al., 2022). In this regard, potential comparison of structure evolution and maximization of energy recovery during CC and CLC is needed.

The present work aims to investigate the reactivity of Cu/CeO$_2$ samples used in CC and CLC processes, the structure evolution behavior of catalysts/OCs, the active interface between the copper species of the catalyst/OCs and the reactive oxygen species and the way of energy recovery. The reaction mechanisms, especially the quantification of reaction rate per active site, are separated using pressure swing adsorption (PSA) of CO and in-situ infrared spectra (IR), which is useful for understanding the reaction behaviors associated with the evolution of lattice oxygen, chemical composition, crystalline phase and structure. In particular, the SEM experiments clearly determined the behavior of structural evolution in both combustion and the migration path of lattice oxygen, which facilitates the understanding of the extent of the contribution of lattice oxygen to the reaction mechanism. In addition, the exergy analysis methodologies are employed to explore the variation of bed temperature field, revealing the reasons for the heat recovery and utilization methods and the loss of available work. These results demonstrate the effective conversion and energy recovery of CO → CO_2 in CC/CLC, and are also helpful to accept these technologies on the treatment of off-gases from steel production.

2. Experimental sections

2.1. Synthesis of catalysts/oxygen carriers

Nanosphere (CeO$_2$–S) and nanorod (CeO$_2$-R) cerium dioxide carriers were supplied by Liaoning KeLong Fine Chemical Co., LTD, P R China. The sol-gel method was used to deposit Cu onto the surface of CeO$_2$ support. To achieve 1.0, 3.0 and 6.0 wt% Cu/Ce, the desired amount of Cu(NO$_3$)$_2 \cdot$3H$_2$O were dissolved in ethanol with magnetic stirring. The required amount of Ce–S or Ce–R support was also added to the Cu (NO$_3$)$_2$ solution and stirred at 80 °C for 12 h. The resulting emulsions were aged at ambient temperature for 12 h, and then transferred to an air drying oven at 105 °C for 12 h, until the ethanol completely evaporated, and calcined in a muffle furnace at 550 °C for 4 h. The prepared samples are denoted as 1Cu/Ce–R, 3Cu/Ce–R, 6Cu/Ce–R, 1Cu/Ce–S, 3Cu/Ce–S and 6Cu/Ce–S, respectively.

2.2. Characterization

Patterns of X-ray diffraction (XRD) were acquired using an XD-3-automatic diffractometer (PERSEE) and a CuKα (λ = 0.15418 nm) radiation source. N_2 adsorption was collected by a U.S. Micromeritics 3 Flex analyzer. X-ray photoelectron spectroscopy (XPS) measurements with a Kratos Axis Ultra DLD spectrometer. Scanning electron microscopy (SEM) experiments were performed using a Hitachi S-4800 electron microscope. High-resolution transmission electron microscopy (HRTEM) images were collected on an FEI Tecnai G^2 F20 transmission microscope. Temperature-programmed reduction by hydrogen (H$_2$-TPR) was conducted by a chemisorption analyzer (TP5080B). 50 mg sample was pretreated in Ar flow at 300 °C for 1 h before being reduced. Then, the sample was heated to 600 °C in 5 vol% H$_2$/Ar flow with a ramp rate of 10 °C/min. In situ infrared spectra (IR) were recorded on a FOLI10-R spectrophotometer conjunction with a self-developed magnetically driven transmission cell, where about 5 mg of sample and 50 mg of KBr were uniformly mixed and pressed into wafers. To eliminate impurities, the catalyst was heated in an Ar gas stream at

300 °C for 1 h. Infrared spectra were collected as background for this catalyst as the temperature was lowered from 300 °C to ambient temperature under the Ar stream. Subsequently, the spectra were collected by passing 10 vol% CO+21 vol% O_2/Ar and 10 vol% CO/Ar atmosphere, respectively, in a continuous flow reaction process heated from 30 °C to 500 °C at a heating rate of 10 °C/min. Adsorption/desorption equilibrium measurements of CO over the samples were recorded by the pressure swing adsorption (PSA) method on an Intelligent Gravimetric Analyzer (IGA-002, Hiden). Before the test, about 60 mg samples were degassed overnight at 120 °C in a vacuum.

2.3. Activity test of CC and CLC

The activity test was evaluated using a fixed-bed plug flow reactor (inner diameter 4 mm) loaded with 200 mg sample during CC and CLC processes. Total flow rates, including CO, O_2 and Ar were controlled at 200 mL/min by flow controllers, corresponding to a GHSV of 19200 h^{-1}. The reaction temperature was firstly programmed from 30 to 300 °C with a heating rate of 10 °C/min, and the temperature was detected by three thermocouples (diameter 0.5 mm) located directly into the center, up-and down-stream to the bed. Then, each sample was tested for three-five cycles at steady state reactions at 50, 300 and 500 °C during CC and CLC, respectively. The effluent CO, O_2 and CO_2 were analyzed via an online mass spectrometer (MS, Pfeiffer OmnistarTM).

3. Results and discussion

3.1. Activity of CC and CLC

The activity of samples was assessed in both CC and CLC processes (Fig. 1). In the CC process, CO was mixed with O_2 and then passed into the furnace to react. All the samples show excellent catalytic performance. Cu/Ce–R is more active than Cu/Ce–S under the same copper loading ratio. The ignition temperature T_{10} (corresponding to 10 vol% CO conversion) of these samples follow the order: 3Cu/Ce–R (57 °C) > 3Cu/Ce–S (60 °C) > 1Cu/Ce–R (62 °C) > 1Cu/Ce–S (67 °C) > 6Cu/Ce–R (72 °C) > 6Cu/Ce–S (75 °C). Further increasing the amount of copper (>3.0 wt%) is unnecessary in T_{10}. The ignition curves display three main steps with the temperature increasing in CC. For example, 3Cu/Ce–R, in the first stage, is a slow induction process that starts at approximately 52 °C and grows at a relatively slow rate to 57 °C. This stage is mainly constrained by dynamic factors. The reaction rate in the second stage is controlled by internal diffusion, manifested as a transient ignition
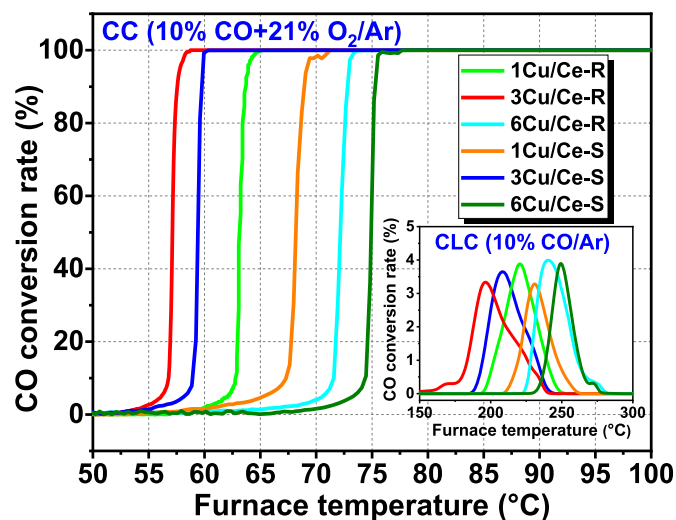
initiated at the gas-solid interface within the temperature range of 57–59 °C. The reaction rate in the third stage is mainly controlled by external diffusion, and the main feature of this stage is that the temperature range is greater than the ignition zone (>59 °C). The activity sequence of Cu/Ce–R and Cu/Ce–S in CLC is consistent with that in CC, but the activation of samples requires a higher reaction temperature than that in CC since no external gaseous O_2 is added. Therefore, self-sustained combustion is unable to achieve since the active lattice oxygen is gradually consumed while not replenished by external gaseous O_2. As a result, the activity curves of CLC for all the samples show a typical "volcano tendency", which implies a low combustion rate with a CO conversion of less than 4%. The line integral method is used to calculate the active lattice oxygen consumption of CLC in each catalyst, which is 1Cu/Ce–R (22.24), 3Cu/Ce–R (24.22), 6Cu/Ce–R (23.39), 1Cu/Ce–S (16.33), 3Cu/Ce–S (22.90), 6Cu/Ce–S (21.54). The calculation results show that the lattice oxygen fluidity of the rod-shaped catalyst is generally greater than that of the spherical catalyst, and there is a positive correlation trend with the loaded Cu content, that is, adding an appropriate amount of Cu can promote the reaction between lattice oxygen and CO.

The evolution of CC and CLC was proved by using 3Cu/Ce–R samples with the best activity combined with the transformation of Step response signals (Fig. 2). For CC, CO is not oxidized at 50 °C as predicted since the furnace temperature is lower than T_{10} but is completely converted to CO_2 at 300 and 500 °C. Four-cycle studies at 300 and 500 °C verified this stable combustion, with no discernible variation in the location and shape of the CO, O_2 and CO_2 concentration curves. With respect to CLC, four-cycle performances are carried out (Fig. 2b), where each cycle consists of introducing 10 vol% CO/Ar (200 ml/min) into the samples for 900 s reduction, and then introducing 21 vol% O_2/Ar (200 ml/min) for 900 s oxidation. The activity of oxygen carriers is reduced in each cycle at 300 and 500 °C, which is indicated in step feeding CO leading to less formation of CO_2, corresponding to the content of active lattice oxygen decreasing from 11.0 to 9.1 mmol/g_{cat} at 300 °C and from 15.9 to 9.6 mmol/g_{cat} at 500 °C through the integration of CO_2 concentration signal. Similarly, the O_2 concentration is also decreased due to the oxidation of Cu^0 to Cu^+ over the successive reaction cycles during CLC. The strong bond binding between CO and the surface of metal oxides depends on the electrons being provided from the surface cations in the opposite direction to the anti-bonding-orbital, which are usually provided by the d-orbital of the metal. Since the outer shell electron distribution of Cu^+ and Cu^{2+} are 3d10 and 3d9, respectively, and the d-orbitals are almost completely filled with electrons, both Cu^+ and Cu^{2+} tend to establish bonds with CO, and the former forms stronger bonds.

Fig. 1. CC and CLC activity curves of Cu/Ce–R and Cu/Ce–S under different copper contents.
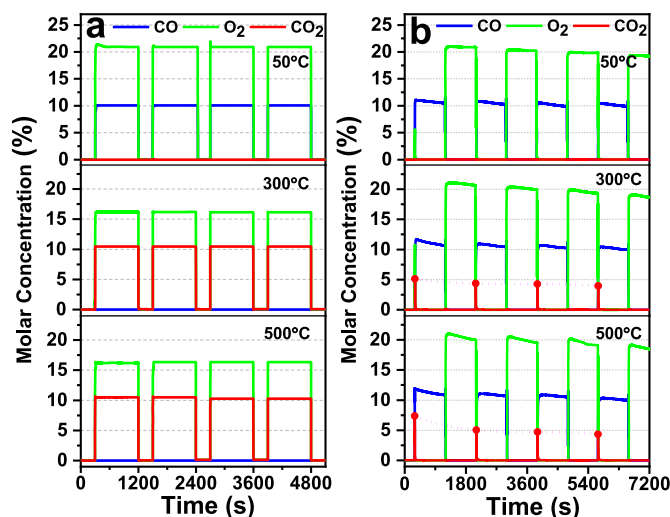

Fig. 2. CC (a) and CLC (b) over 3Cu/Ce–R at different temperatures with time.

To gain a clear understanding of the changes in the structure and physicochemical properties of the samples in CC and CLC, fresh and used samples are thoroughly evaluated and are discussed in the following sections.

3.2. Physicochemical characterization

The crystal structure of all samples was identified by XRD. As shown in Fig. S1 of the Supplementary materials, the fluorite cubic CeO_2 is the only observed phase in Ce–R, Ce–S and all modified Cu/Ce samples at 2θ = 28.5, 33.1, 47.5 and 56.5°, corresponding to (111), (100), (220) and (311) crystal faces (JCPDS 34–0394), respectively (Spezzati et al., 2019; Yuan et al., 2023). No CuO characteristic peaks could be found due to the limitation of XRD detection since either $CuCeO_x$ solid solutions are formed, or copper is highly dispersed in the form of CuO_x clusters on the ceria support. It is clearly found that the Ce–R, Ce–S, Cu/Ce–R and Cu/Ce–S samples are similar in lattice parameters (Table 1). Note that the diffraction peaks of Cu/Ce–R samples are higher intensity, suggesting a higher crystallite size (Table 1) than those of Cu/Ce–S, corresponding to the lower BET areas confirmed by N_2 adsorption (Table 1). The diffraction peaks for 3Cu/Ce–R and 3Cu/Ce–S are almost retained after CC and CLC, but 3Cu/Ce–S exhibits a stronger intensity, attributed to agglomeration and crystallization after CLC.

HRTEM and SEM analyses were performed to investigate the structural characteristics of fresh and used 3Cu/Ce–R and 3Cu/Ce–S samples (Fig. 3), with the 3D reconstruction of the surface morphology of the samples. Concerning HRTEM images, 3Cu/Ce–R is dominated by (100) crystal faces (Fig. 3a), with an interplanar spacing of 0.265 nm. The 3Cu/Ce–S surface consists mainly of (111) crystal faces (Fig. 3h) with a crystalline spacing of 0.313 nm (Dong et al., 2022). Since no other diffraction rings as well as separate reflections of CuO were detected, this confirms that it exists mainly in the amorphous form (am-CuO_x). Cerium oxide with shape specificity is exposed to different surfaces, making it possible to investigate the relationship between activity and specific morphology experimentally. Compared with (111) crystal surface, (100) crystal surface has a lower Ce–O binding energy, thus exhibiting a better activity (Liang et al., 2022), consistent with the activity shown in Fig. 1. For SEM images, the fresh 3Cu/Ce–R consists of distinct rods with an average diameter of 200 nm (Fig. 3b). 3Cu/Ce–S (Fig. 3i) consists of spheres with an average diameter of 150 nm, and the reconstructed image has relatively uniform colors. Fig. 3c and j shows the catalytically burned 3Cu/Ce–R and 3Cu/Ce–S with slightly rougher surfaces compared to their corresponding fresh samples but still maintaining their respective shapes. This is due to the fact that the release of

lattice oxygen in the reaction can be supplemented in time by gas-phase oxygen. The red site in the reconstructed image color indicates that this is the phase interface of the active reaction. Therefore, the catalyst shows high activity and stability in CC, as confirmed in Fig. 2a. However, both the 3Cu/Ce–R and 3Cu/Ce–S structures underwent severe sintering after several CLC cycles, as observed by SEM (Fig. 3d and k), and were unable to achieve significant surface reconstruction, which is consistent with the XRD results. In this case, the samples can never be re-oxidized to their original state after gaseous oxygen is introduced. This is the culprit for the decrease in activity after CLC (Fig. 2b).

To determine the chemical states and compositions of 3Cu/Ce–S and 3Cu/Ce–R before and after CC/CLC, XPS analysis was performed. For the Cu 2p spectra (Fig. S2a, Supplementary materials), two characteristic peaks could be observed for Cu $2p_{3/2}$, i.e. the Cu$^+$ state located at 933.4 eV and Cu^{2+}_2/CuO species centered at 935.0 eV with broad shake-up peaks around 938–948 eV (Conradie and Erasmus, 2022). The spectrum of the Ce 3d region can be divided into eight peaks (Fig. S2b, Supplementary Material), consisting of two sets of peaks with overlapping spin orbitals, corresponding to $3d_{3/2}$ labeled as u (u-u_3) and $3d_{5/2}$ labeled as v (v-v_3), respectively. The u_1 (903.0 eV) and v_1 (884.7 eV) peaks are designated as Ce^{3+} and the remaining peaks correspond to Ce^{4+} states (Yu et al., 2018). Surface atomic ratios of samples calculated according to the peak area ratios are listed in Table 2. Quantitative data suggest Ce^{3+}/Ce ratios of 11.5% for 3Cu/Ce–R and 10.7% for 3Cu/Ce–S, which are higher than CeO_2-R and CeO_2-S. The presence of Ce^{3+} in the samples favors the formation of vacancies and unsaturated chemical bonds on the catalyst/OCs surface. Due to the stable structure of rod-shaped catalysts, the ratios of Cu/Ce, Ce^{3+}/Ce and Cu^+/Cu remained almost unchanged compared with the fresh samples before and after CC/CLC. However, the Cu^+/Cu ratios of spherical-shaped samples increased from 39.8% to 43.7% and 47.5% after CC and CLC, respectively, since the elemental copper oxidation is more difficult to occur than the CuO_x reduction at a specific temperature. Due to the high specific surface area of spherical-shaped samples, the copper can be better dispersed on the external surface of catalyst/OCs, leading to lower Cu/Ce ratios than the rod-shaped samples. Because the thermal variation and ageing effects play important roles in alternating redox and oxidation cycles of CLC, the instability of spherical-shaped samples, which has been confirmed by HRTEM, leads to relative migration of copper elements onto the external surface implying elevated Cu/Ce. In addition, the ratio of copper to cerium concentration in 3CuCe-R and 3CuCe–S bulk phases determined via atomic absorption spectroscopy in PerkinElmer AAnalyst 300 (AAS) was 6.65 (where the Cu: Ce atomic ratio follows the chemical equivalence ratio), which is much smaller than the value detected by XPS. This is because XPS is a surface technology that prioritizes the detection of species located on surface samples (sampling depths of approximately 3–10 nm), indicating the enrichment of Cu on the CeO_2 surface.

3.3. H_2-TPR analysis

In Fig. 4, the results of the H_2-TPR tests were shown to illustrate the reducibility of catalysts. The total amounts of H_2 consumed are listed in Table 1. Considering cerium species with low reducibility demonstrated by our previous work (Kang et al., 2021), the H_2-TPR profiles exhibit two reduction peaks, labeled as α and β, below 300 °C, which are correlated with the reduction of interface oxygen from Cu-O_x-Ce, and highly dispersed CuO_x species interacted with ceria supports, respectively. Mixed oxides lead to the formation of coordination unsaturated species, which is beneficial for increasing the fluidity of oxygen. With the loading ratio of copper increased from 1% to 3%, both reduction peaks shift towards the low-temperature direction, and the H_2 uptake also increases. The surface enrichment of copper was detected using XPS, indicating that copper species preferentially cover the highly dispersed cerium phase. With further increasing the copper loading ratio to 6%, however, both α and β reduction peaks shift moderately back to

Table 1
Lattice parameters and crystal size by XRD, BET area by N_2 adsorption and H_2 consumption by H_2-TPR.

Samples	Lattice parameter[a] (nm)	Crystal size[b] (nm)	BET area (m²/g)	H_2 consumption (mmol/g)		
				α	β	Total
CeO_2-R	0.5409	47.60	26.76	/	/	/
1Cu/Ce–R	0.5403	52.74	26.28	3.0	2.3	5.4
3Cu/Ce–R	0.5411	53.84	26.16	4.3	5.9	10.3
6Cu/Ce–R	0.5411	52.98	24.89	2.0	2.8	4.8
CeO_2-S	0.5403	13.22	111.47	/	/	/
1Cu/Ce–S	0.5412	15.12	87.19	1.4	5.3	6.7
3Cu/Ce–S	0.5414	14.75	84.88	4.0	5.8	9.8
6Cu/Ce–S	0.5412	14.00	80.55	2.0	2.3	4.3

[a] For fluorite phase, calculated by the Bragg equation ($2d \sin\theta = n\lambda$).
[b] Based on Scherrer equation using the (111) peaks.

Fig. 3. HRTEM images of fresh 3Cu/Ce–R (a) and 3Cu/Ce–S (h); SEM images and 3D reconstructions of fresh 3Cu/Ce–R (b,e), 3Cu/Ce–S (i,l), used 3Cu/Ce-R-CC (c, f), 3Cu/Ce-R-CLC (d,g), 3Cu/Ce-S-CC (j,m), 3Cu/Ce–S-CLC (k,n).

Table 2
Surface atomic ratios were obtained by XPS method analysis.

Samples	Surface atomic ratio (%)		
	Cu/Ce	Cu^+/Cu	Ce^{3+}/Ce
CeO_2-R	/	/	6.8
CeO_2–S	/	/	6.4
3Cu/Ce–R	55.1	39.7	11.5
3Cu/Ce–S	35.6	39.8	10.7
3Cu/Ce-R-CC	54.8	36.3	11.9
3Cu/Ce-S-CC	34.2	43.7	11.1
3Cu/Ce-R-CLC	57.3	38.7	10.6
3Cu/Ce-S-CLC	47.9	47.5	9.6

higher temperatures, and the H_2 uptake decreases simultaneously, which can be attributed to the aggregation of copper species. The reducibility of catalysts is mainly dependent on the location of the low-temperature reduction peak rather than the H_2 consumption, thus determining their activity. The redox properties of 3Cu/Ce–R and 3Cu/Ce–S after CC and CLC were also studied (Fig. S3, Supplementary materials). Compared with the fresh samples, the α peak showed a slight decrease and the β peak increased instead, but no apparent shift of peaks can be observed. After multiple CLC cycles, the copper of OCs is migrated as +1 valence and enriched on the surface irreversibly, resulting in sintering, crystallization and agglomeration of materials, which increases the reduction temperature and reduces the H_2 consumption inevitably. The number of active sites exposed on the catalyst surface plays a particularly important role in CO oxidation, as more
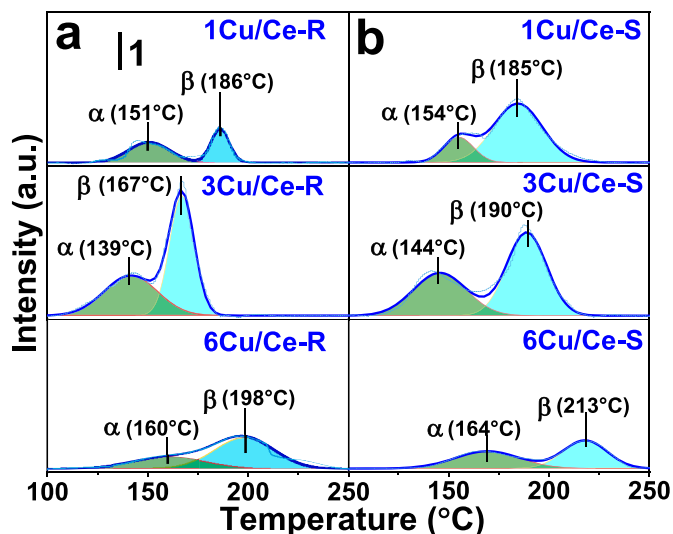
Fig. 4. H_2-TPR profiles of Cu/Ce–R (a) and Cu/Ce–S (b).

active sites can promote the participation of more CO and O_2 in the reaction. Despite the large difference in the specific surface areas of CuCe-R and CuCe–S catalysts, the H_2-TPR results showed a small difference in the content of major active species between CuCe-R and CuCe–S catalysts, with 3CuCe-R catalysts having a higher content of

surface-active species than 3CuCe–S.

3.4. In situ IR spectra and PSA test

As shown in Fig. 5, the CO reaction mechanism of CC and CLC using the optimal 3Cu/Ce–R catalyst was explored through in situ IR. During CC and CLC, the gaseous CO and adsorbed CO (carbonyls, Cu + -CO), respectively, are assigned to the absorption bands at 2174 and 2118 cm^{-1} (Kang et al., 2023). The electron donation from carbon (lone pair on 5σ orbital) to the metal cations' (Cu$^+$) d-orbitals and the electron back-donation from the metal cations to carbon's (2π*-antibonding) d-orbitals both contribute to the adsorbed CO on 3Cu/Ce–R (Wu et al., 2018). The outer layer electron distribution of The Ce^{3+} and Ce^{4+} is 4f1 and 5S2 4d10 5P6, respectively. Such Electron shell distribution is difficult to provide electrons from d-orbitals to CO anti-bonding π-orbitals. Due to the weak interaction between adsorbed CO and O$_2$, the intensity peak for carbonate species is quite weak at 1350-1750 cm^{-1} in the CC process (Fig. 5a), whereas for CLC, no carbonate species are formed due to the lack of O$_2$ (Fig. 5c). The intensity of the CO band decreased fast as the temperature increased from 30 to 500 °C, with no discernible change in the carbonate (Fig. 5a and b). Simultaneously, the active lattice oxygen of the 3Cu/Ce–R system effectively reacts with CO adsorbed on the catalyst surface, leading to an increase in the signal intensity of CO$_2$ (2342 and 2361 cm^{-1}). Therefore, the reaction between carbonyls and lattice oxygen is a significant contributor to CO oxidation rather than the decomposition of carbonates. Compared with the CLC process (Fig. 5c and d) under 10 vol% CO/Ar atmosphere, the CC reaction over the 3Cu/CeO$_2$-R catalyst under 10 vol% CO+21 vol% O$_2$/Ar atmosphere yields more CO$_2$ at the lower temperatures, which can be attributed to the higher active oxygen content enhancing the reaction activity. This observation is consistent with the activity results. As such, the CuO$_x$ adsorption sites in the Cu–Ce interface to the adjacent surface lattice oxygen, which is available for the transformation and reaction, becomes an important factor in the activity analysis of 3Cu/CeO$_2$-R during CC.

The adsorption and desorption isotherms of CO were conducted by the PSA method to further investigate the surface chemical properties of materials, with the results displayed in Fig. 6a. Both the 3Cu/Ce–R and 3Cu/Ce–S adsorption isotherm curves can be categorized as type I according to the IUPAC classification, indicating a strong interaction between catalyst/OCs surface and CO (Oh et al., 2022). Most importantly,
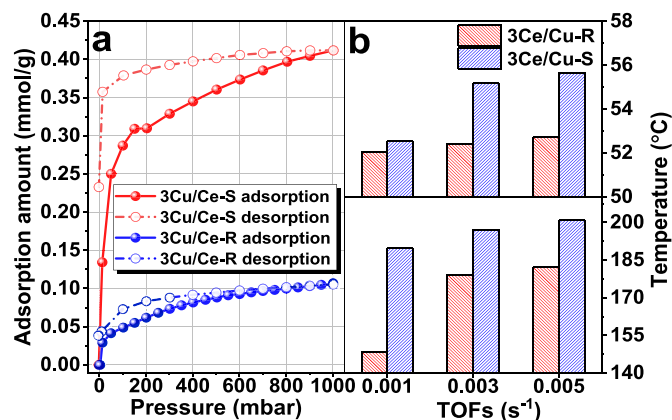

Fig. 6. Adsorption amount of CO at 25 °C (a) and TOFs (b) over 3Cu/Ce–R and 3Cu/Ce–S.

the desorption isotherm cannot coincide with the adsorption isotherm, and the difference suggests the chemical adsorption of CO on the active sites to form carbonyls (Cu$^+$–CO) as described in the IR. Considering that the quantities of 3Cu/Ce–R and 3Cu/Ce–S tested are 58.035 and 59.848 mg, the saturated adsorption capacity of CO are calculated as 0.106 and 0.412 mmol/g$_{cat}$ respectively at 1000 mbar, where their obvious difference shows a significant positive correlation with BET area. Such an adsorption capacity is obviously lower than that determined by step-response runs, and therefore the redox cycle has penetrated into its bulk phase and is no longer limited to the material surface, which accelerates the Cu$^+$ enriched on the surface, sintering and agglomeration of materials. The turnover frequencies (TOFs) are calculated based on CO conversion (<4% during CC and CLC where the reaction is kinetically regulated, Fig. 1) divided by the numbers of active sites and listed in Fig. 6b. The 3Cu/Ce–R shows the same TOFs at lower temperatures compared with 3Cu/Ce–S at higher temperatures. Evidently, such superb activity obtained for 3Cu/Ce–R depends mainly on (100) crystal faces rather than the BET area. Since the active oxygen is replenished in time, the CC obtains the same reaction rate at a lower temperature than CLC.
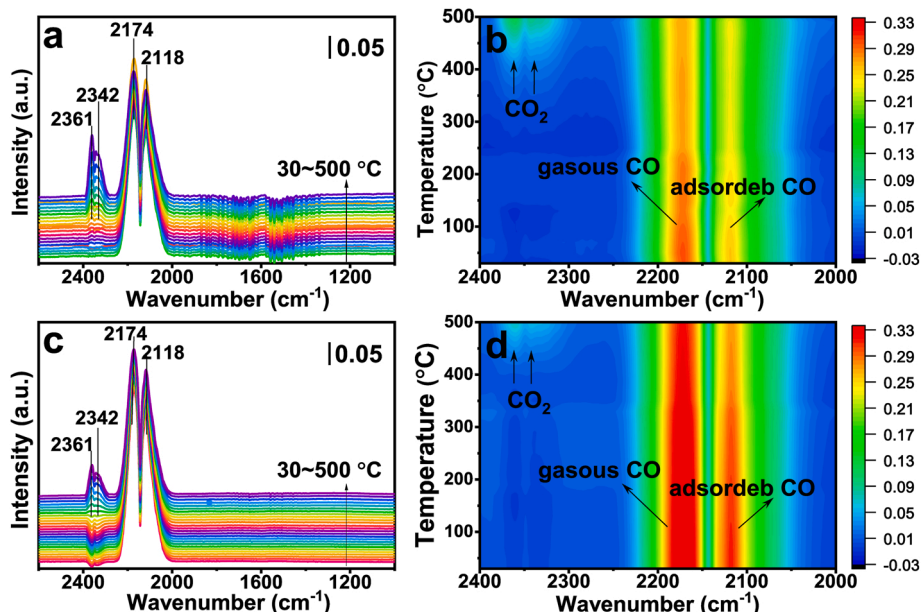

Fig. 5. In situ IR experimental results of fresh 3Cu/Ce–R under CC (a, b) and CLC continuous flow.

3.5. Thermodynamic analysis

Fig. 7 shows the comparison of the energy utilization efficiency under CC and CLC. For CC, the furnace was heated at a rate of 10 °C/min while introducing a mixture of 3 vol% CO+21 vol% O₂/Ar. It can be seen that CO was ignited after 200s. Fig. 1 has testified that there is an obvious warming process of adiabatic combustion temperature and bed temperature with the CO conversion rate increasing. After 700s, the heating in the electric furnace was stopped and the furnace door was opened. Then the adiabatic combustion temperature, bed temperature and tail gas temperature decreased until they stabilized after 1000s. At this point, the bed temperatures were maintained at 330 °C. The adiabatic combustion temperature under this condition is calculated to be 390 °C. Since thermochemical runaway cannot occur in CLC, however, it was ignited by gas transient switching at the constant temperature of 500 °C. Upon introducing 3 vol% CO/Ar, the temperature rises sharply to 547 °C and then falls back to 513 °C. This may be caused by the rapid consumption of the surface-active oxygen and the pulling out of internal lattice oxygen of OCs. The electric furnace was turned off after 500s. Although CO was still introduced at this moment, unlike CC combustion, the bed temperature could not be maintained and then fell to room temperature. Obviously, investigation related to the exothermic differences between CC and CLC at low CO concentrations should not only be beneficial to the potential energy utilization, but also promote rational burner design and safety assessment. The shaded area (Fig. 7) refers to the heat release of CC and CLC after combustion stabilization, corresponding to the time average heat release power calculated as 1.04 and 0.04 W, respectively. Although the exothermic power of CC is relatively high at this time, according to the exergy efficiency calculation formula, the exergy efficiency of CC and CLC are 54% and 62%, respectively. This indicates that the irreversible loss of CLC during combustion is relatively small.

$$\eta = \frac{E_n}{E_F} \quad (1)$$

$$E_F = \sum_i X_i E_{Fi} + \overline{R} T_0 \sum_i X_i \ln X_i \quad (2)$$

$$E_n = I_n \left(1 - \frac{T_0}{T_f} \times \ln - \frac{T_f}{T_0} \right) \quad (3)$$
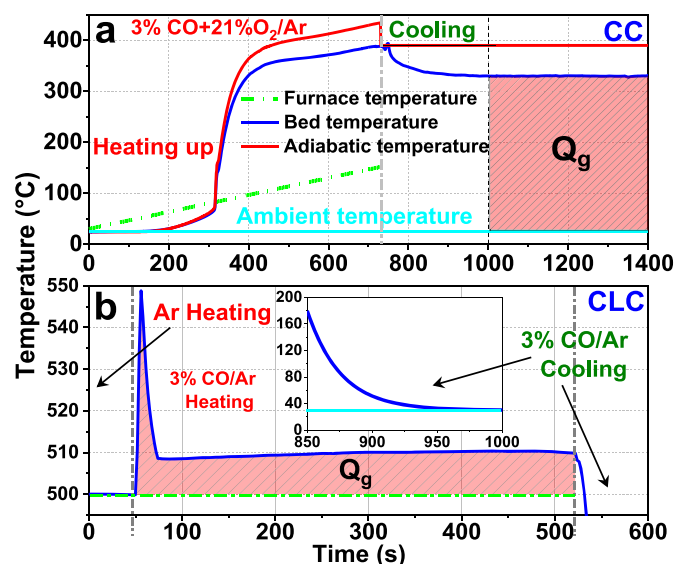
where E_F is the chemical exergy;

E_n is exergy of combustion products
T_0 is the ambient temperature
T_f is the adiabatic combustion temperature

The critical equivalence ratio (φ_C) of CO self-sustained combustion was finally determined to reveal the law of energy recovery and utilization of low CO concentration, which was investigated at different flow rates using the dichotomous method (Huang et al., 2021). The results are shown in Fig. 8a. Due to its excellent activity, which most readily results in the production of local hot spots on the catalyst surface and consequently only requires a low stoichiometric ratio to give a suitable local temperature for its ignition, 3Cu/Ce–R has the lowest φ_C under the same flow rate. However, no simple monotonic relationship exists between flow rate and φ_C. When the flow rate is increased, the φ_C initially declines and then increases, reaching its minimum at 200 ml/min 3Cu/CeO₂-R, which shows the best activity, was chosen to investigate this phenomenon. Fig. 8b shows that at low flow rates, the heat released from the small amount of CO cannot sustain the combustion. As a result, a large concentration of CO is required, which inevitably leads to an increase of adiabatic combustion temperature at this point and correspondingly an increase in the loss of steam. At a high flow rate, the increase of gas-bed heat exchange results in a substantial amplification between the adiabatic combustion temperature and bed temperature at this point, and the exergy destroyed also increases. Therefore, a high CO concentration is required to resist blowing out. Although the φ_C increases with flow rate, it is clear that the φ_C for all the catalysts tested are outside the lean limit of conventional flame combustion mode.

4. Conclusion

In this paper, the sol-gel method was used to load CuO on CeO₂ carriers with regular morphology to explore its reactivity, structural evolution of catalyst/OCs and energy recovery in CC and CLC processes. At an optimum Cu content of 3%, the rod-shaped samples exhibited higher activity than the spherical samples. The CO adsorbed on Cu⁺ at the Cu–Ce interface reacts with the adjacent surface lattice oxygen, which is the main reason for the strong exotherm during the CC process and maintains the self-sustaining combustion of CO. No significant evolution of the catalyst chemistry, crystalline phase and structure is observed, as the surface lattice oxygen of the material is continuously replenished by gas-phase oxygen. However, the release of lattice oxygen in the CLC process cannot be replenished in time, and therefore the oxidation rate of CO is lower than that of the CC process. Moreover, the CLC process leads to Cu⁺ enrichment on the sample surface as well as irreversible sintering and agglomeration of the material (see Fig. 9) ultimately leading to a decrease in the activity of OCs, which happens to be
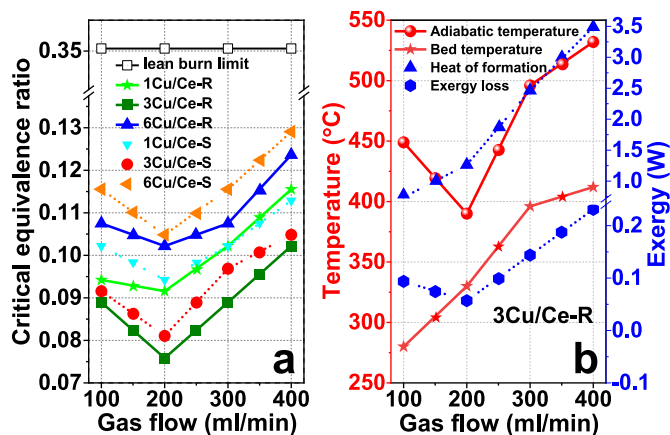

Fig. 7. Heat transfer of low CO concentration in CC (a) and CLC (b).

Fig. 8. Limits of CC at CO lean conditions (a) and the exergy versus flow rate (b).
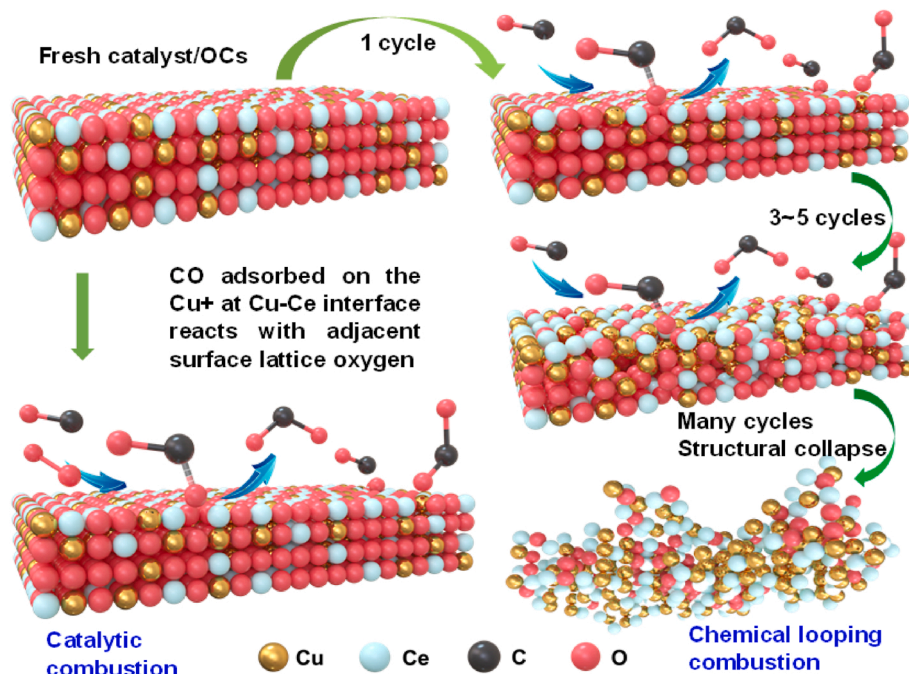
Fig. 9. Routes for the reactions of CC and CLC.

one of the current challenges for the application of the CLC process. In terms of energy recovery although CC exhibits faster heat release per unit time than CLC, it has lower exergy efficiency and larger exergy loss. In addition, the effect of flow rate on exergy loss is not linear, and there exists a local minimum for the exergy loss at around 200 ml/min, after which the exergy loss shows an increase trend with the increase of flow rate.

CRediT authorship contribution statement

Junqin Huang: Writing – original draft, Writing – review & editing, Software. **Huan Liu:** Methodology. **Chenhang Zhang:** Visualization, Investigation. **Feng Bin:** Conceptualization, Writing – review & editing, Supervision, Funding acquisition. **Xiaolin Wei:** Project administration. **Running Kang:** Formal analysis. **Shaohua Wu:** Writing – review & editing.

Declaration of competing interest

The authors declare that they have no known competing financial interests or personal relationships that could have appeared to influence the work reported in this paper.

Data availability

The authors do not have permission to share data.

Acknowledgement

Appendix A. Supplementary data

Supplementary data to this article can be found online at https://doi.org/10.1016/j.jclepro.2023.138038.

References

Adánez, J., Abad, A., 2019. Chemical-looping combustion: status and research needs. Proc. Combust. Inst. 37, 4303–4317. https://doi.org/10.1016/j.proci.2018.09.002.

Bin, F., Kang, R., Wei, X., Hao, Q., Dou, B., 2019. Self-sustained combustion of carbon monoxide over $CuCe_{0.75}Zr_{0.25}O_\delta$ catalyst: stability operation and reaction mechanism. Proc. Combust. Inst. 37, 5507–5515. https://doi.org/10.1016/j.proci.2018.05.114.

Chen, L., Wei, G., Liu, K., 2022. Influences of reaction and thermal conditions on microstructural evolutions of ilmenite oxygen carriers for chemical looping combustion. Fuel Process. Technol. 228, 107139 https://doi.org/10.1016/j.fuproc.2021.107139.

Chen, W., Xu, J., Huang, F., Zhao, C., Guan, Y., Fang, Y., Hu, J., Yang, W., Luo, Z., Guo, Y., 2023. CO oxidation over CuO_x/TiO_2 catalyst: the importance of oxygen vacancies and Cu^+ species. Appl. Surf. Sci. 618, 156539 https://doi.org/10.1016/j.apsusc.2023.156539.

Cho, P., Mattisson, T., Lyngfelt, A., 2005. Carbon Formation on nickel and iron oxide-containing oxygen carriers for chemical-looping combustion. Ind. Eng. Chem. Res. 44, 668–676. https://doi.org/10.1021/ie049420d.

Conradie, J., Erasmus, E., 2022. XPS photoelectron lines, satellite structures and Wagner plot of Cu(II) β-diketonato complexes explained in terms of its electronic environment. J. Electron. Spectrosc. Relat. Phenom. 259, 147241 https://doi.org/10.1016/j.elspec.2022.147241.

Dong, J., Hu, Q., Liu, H., Wu, Y., Ma, Z., Fan, Y., Li, R., Xu, J., Wang, X., 2022. 3D flower-like Ni doped CeO_2 based gas sensor for H_2S detection and its sensitive mechanism. Sensor. Actuator. B Chem. 357, 131227 https://doi.org/10.1016/j.snb.2021.131227.

Gao, Y., Hu, E., Yi, Y., Yin, G., Huang, Z., 2023. Plasma-assisted low temperature ammonia decomposition on 3d transition metal (Fe, Co and Ni) doped CeO_2 catalysts: synergetic effect of morphology and co-doping. Fuel Process. Technol. 244, 107695 https://doi.org/10.1016/j.fuproc.2023.107695.

Hua, Q., Cao, T., Bao, H., Jiang, Z., Huang, W., 2013. Crystal-plane-controlled surface chemistry and catalytic performance of surfactant-free Cu_2O nanocrystals. ChemSusChem 6, 1966–1972. https://doi.org/10.1002/cssc.201300376.

Huang, J., Teng, Z., Kang, R., Bin, F., Wei, X., Hao, Q., Nam Hui, K., San Hui, K., Dou, B., 2021. Study on activity, stability limit and reaction mechanism of CO self-sustained combustion over the $LaMnO_3$, $La_{0.9}Ce_{0.1}MnO_3$ and $La_{0.9}Sr_{0.1}MnO_3$ perovskite catalysts using sugar agent. Fuel 292, 120289. https://doi.org/10.1016/j.fuel.2021.120289.

Igalavithana, A.D., Choi, S.W., Dissanayake, P.D., Shang, J., Wang, C.-H., Yang, X., Kim, S., Tsang, D.C.W., Lee, K.B., Ok, Y.S., 2020. Gasification biochar from biowaste (food waste and wood waste) for effective CO_2 adsorption. J. Hazard Mater. 391, 121147 https://doi.org/10.1016/j.jhazmat.2019.121147.

Jia, G., Ling, L., Zhang, R., Wang, B., 2022. The effect of ferromagnetism on the CO activation over FCC crystal phase transition metal catalysts: insights from DFT calculations. Mol. Catal. 518, 112071 https://doi.org/10.1016/j.mcat.2021.112071.

Kang, R., Ma, P., He, J., Li, H., Bin, F., Wei, X., Dou, B., Hui, K.N., Hui, K.S., 2021. Transient behavior and reaction mechanism of CO catalytic ignition over a $CuO–CeO_2$ mixed oxide. Proc. Combust. Inst. 38, 6493–6501. https://doi.org/10.1016/j.proci.2020.06.186.

Kang, R., Zhang, Z., Bin, F., Wei, X., Li, Y., Chen, G., Tu, X., 2023. Catalytic ignition of CO over CuCeZr based catalysts: new insights into the support effects and reaction pathways. Appl. Catal., B 327, 122435. https://doi.org/10.1016/j.apcatb.2023.122435.

Kim, J., Sovacool, B.K., Bazilian, M., Griffiths, S., Lee, J., Yang, M., Lee, J., 2022. Decarbonizing the iron and steel industry: a systematic review of sociotechnical systems, technological innovations, and policy options. Energy Res. Social Sci. 89, 102565 https://doi.org/10.1016/j.erss.2022.102565.

Lian, Z., Li, F., He, X., Chen, J., Yu, R.-C., 2022. Rising CO_2 will increase toxicity of marine dinoflagellate Alexandrium minutum. J. Hazard Mater. 431, 128627 https://doi.org/10.1016/j.jhazmat.2022.128627.

Liang, W., Li, X., Ju, H., Ren, S., 2022. Adsorption and dissociation mechanism of toluene on Pd (111) and PdO (101) surface: first principle calculation. Surf. Sci. 720, 122051 https://doi.org/10.1016/j.susc.2022.122051.

Lin, Y., Wang, H., Wang, Y., Huo, R., Huang, Z., Liu, M., Wei, G., Zhao, Z., Li, H., Fang, Y., 2020. Review of biomass chemical looping gasification in China. Energy Fuels 34, 7847–7862. https://doi.org/10.1021/acs.energyfuels.0c01022.

Liu, H., Li, C., Yuan, J., Xiang, K., Shen, F., Yang, W., 2023a. Cu-CeO$_2$ nanorings with abundant oxygen vacancies for superior catalytic oxidation. Mater. Lett. 334, 133707 https://doi.org/10.1016/j.matlet.2022.133707.

Liu, H., Li, C., Yuan, J., Xiang, K., Shen, F., Yang, W., 2023b. Cu-CeO$_2$ nanorings with abundant oxygen vacancies for superior catalytic oxidation. Mater. Lett. 334, 133707 https://doi.org/10.1016/j.matlet.2022.133707.

Long, Y., Gu, Z., Lin, S., Yang, K., Zhu, X., Wei, Y., Wang, H., Li, K., 2021. NiO and CuO coated monolithic oxygen carriers for chemical looping combustion of methane. J. Energy Inst. 94, 199–209. https://doi.org/10.1016/j.joei.2020.09.004.

Mrabet, D., Abassi, A., Cherizol, R., Do, T.-O., 2012. One-pot solvothermal synthesis of mixed Cu-Ce-O$_x$ nanocatalysts and their catalytic activity for low temperature CO oxidation. Appl. Catal. Gen. 447–448, 60–66. https://doi.org/10.1016/j.apcata.2012.09.005.

Oh, H., Lee, S., Beum, H.T., Kim, J., Kim, J., Lee, S.-Y., Lee, I.-B., Yoon, Y.-S., Han, S.S., 2022. CO recovery from blast furnace gas by vacuum pressure swing adsorption process: experimental and simulation approach. J. Clean. Prod. 346, 131062 https://doi.org/10.1016/j.jclepro.2022.131062.

Ren, P., Tu, W., Wang, C., Cheng, S., Liu, W., Zhang, Z., Tian, Y., Han, Y.-F., 2022. Mechanism and sites requirement for CO hydrogenation to CH$_3$OH over Cu/CeO$_2$ catalysts. Appl. Catal. B Environ. 305, 121016 https://doi.org/10.1016/j.apcatb.2021.121016.

Spezzati, G., Benavidez, A.D., DeLaRiva, A.T., Su, Y., Hofmann, J.P., Asahina, S., Olivier, E.J., Neethling, J.H., Miller, J.T., Datye, A.K., Hensen, E.J., 2019. CO oxidation by Pd supported on CeO$_2$(100) and CeO$_2$(111) facets. Appl. Catal. B Environ. 243, 36–46. https://doi.org/10.1016/j.apcatb.2018.10.015.

Sun, Z., Russell, C.K., Whitty, K.J., Eddings, E.G., Dai, J., Zhang, Y., Fan, M., Sun, Z., 2023a. Chemical looping-based energy transformation via lattice oxygen modulated selective oxidation. Prog. Energy Combust. Sci. 96, 101045 https://doi.org/10.1016/j.pecs.2022.101045.

Sun, Z., Wang, T., Zhang, R., Li, H., Wu, Y., Toan, S., Sun, Z., 2023b. Boosting hydrogen production via deoxygenation-sorption-enhanced biomass gasification. Bioresour. Technol. 382, 129197 https://doi.org/10.1016/j.biortech.2023.129197.

Wang, L., Peng, H., Shi, S., Hu, Z., Zhang, B., Ding, S., Wang, S., Chen, C., 2022. Metal-organic framework derived hollow CuO/CeO$_2$ nano-sphere: to expose more highly dispersed Cu-O-Ce interface for enhancing preferential CO oxidation. Appl. Surf. Sci. 573, 151611 https://doi.org/10.1016/j.apsusc.2021.151611.

Wu, Q., Zhou, H., 2022. Investigation on the catalytic combustion of CO over LaMn$_{1-X}$Cu$_X$O$_3$ promoted by acid treatment. Asia Pac. J. Chem. Eng. 17, e2728 https://doi.org/10.1002/apj.2728.

Wu, W., Savereide, L.M., Notestein, J., Weitz, E., 2018. In-situ IR spectroscopy as a probe of oxidation/reduction of Ce in nanostructured CeO2. Appl. Surf. Sci. 445, 548–554. https://doi.org/10.1016/j.apsusc.2018.03.083.

Wu, Y., Luo, C., Zhang, X., Zheng, X., Zhu, T., Su, Q., 2020. Utilization of converter off-gas based on a chemical-looping combustion process. Energy Sources, Part A Recovery, Util. Environ. Eff. 42, 2090–2102. https://doi.org/10.1080/15567036.2019.1607928.

Yu, C., Boily, J.-F., Shchukarev, A., Drake, H., Song, Z., Hogmalm, K.J., Åström, M.E., 2018. A cryogenic XPS study of Ce fixation on nanosized manganite and vernadite: interfacial reactions and effects of fulvic acid complexation. Chem. Geol. 483, 304–311. https://doi.org/10.1016/j.chemgeo.2018.02.033.

Yuan, Z., Cao, T., Deng, M., Ma, J., Geng, S., Yang, C., Ren, Y., Yao, M., Liu, F., Wang, X., 2023. Unveiling the CeO$_2$ morphology effect in Pd-CeO$_2$/C heterostructures catalysts for formic acid dehydrogenation. Fuel 346, 128333. https://doi.org/10.1016/j.fuel.2023.128333.

Zhao, Y., Zhang, Y., Cui, Y., Duan, Y., Huang, Y., Wei, G., Mohamed, U., Shi, L., Yi, Q., Nimmo, W., 2022. Pinch combined with exergy analysis for heat exchange network and techno-economic evaluation of coal chemical looping combustion power plant with CO_2 capture. Energy 238, 121720. https://doi.org/10.1016/j.energy.2021.121720.

Zhao, F., Gong, M., Zhang, G., Li, J., 2015. Effect of the loading content of CuO on the activity and structure of CuO/Ce-Mn-O catalysts for CO oxidation. J. Rare Earths 33, 604–610. https://doi.org/10.1016/S1002-0721(14)60460-9.

Zuo, L., Yu, S., Zhang, R., Li, H., Wu, Y., Abiev, R., Sun, Z., Sun, Z., 2023. Tunning Pd–Cu-based catalytic oxygen carrier for intensifying low-temperature methanol reforming. J. Clean. Prod. 410, 137212 https://doi.org/10.1016/j.jclepro.2023.137212.